https://doi.org/10.5194/egusphere-2026-656
Preprint. Discussion started: 22 May 2026

Soil microwave background retrieval and snow sensitivity from multi-frequency SAR observations over an agro-forested environment in northern Ontario

Alex Gélinas[1,2], Benoît Montpetit[3], Julien Meloche[3], Peter Toose[3], Zeinab Akhavan[4], Wei Wang[4], Richard Kelly[4], Alexandre Langlois[2,5], and Alexandre Roy[1,2]

[1]Centre de recherche sur les interactions bassins versants – écosystèmes aquatiques (RIVE), Université du Québec à Trois-Rivières, Trois-Rivières, Canada
[2]Centre d'études nordiques (CEN), Université Laval, Québec, Canada
[3]Climate Research Division, Environment and Climate Change Canada, Toronto, Canada
[4]Department of Geography and Environmental Management, University of Waterloo, Waterloo, Canada
[5]Centre d'Applications et de Recherches en Télédétection (CARTEL), Université de Sherbrooke, Sherbrooke, Canada

Correspondence: Alex Gélinas (alex.gelinas5@uqtr.ca) and Alexandre Roy (alexandre.roy@uqtr.ca)

Abstract. Accurate retrieval of Snow Water Equivalent (SWE) using Synthetic Aperture Radar (SAR) requires effectively decoupling the signal contribution of the snowpack from that of the underlying soil. This study evaluates a multi-frequency soil parameter inversion methodology using the Snow Microwave Radiative Transfer (SMRT) model in a temperate, agro-forested environment in Powassan, Ontario. Using multi-frequency observations from Cryospheric SAR (CryoSAR) (L-band), Radarsat Constellation Mission (RCM) (C-band), and TerraSAR-X (TSX) (X-band) acquired during the 2022/2023 winter season, soil roughness and permittivity were jointly inverted to reproduce observed backscatter. The inversion strategy, which optimizes a single time-invariant roughness per site alongside time-varying permittivity, achieved strong agreement between simulated and observed signals across frequencies (Global $R^2 = 0.87$, RMSE $=1.25\,\mathrm{dB}$). Sensitivity analyses reveal a clear frequency-dependent hierarchy of controls: surface roughness dominates L-band backscatter (particularly in VV polarization), soil permittivity governs C- and X-band responses, and extending the analysis to explicitly include snow properties shows that the dominant controls progressively shift to snow microstructure and depth toward Ku-band. Comparisons with in situ measurements indicate that inverted parameters represent effective values at the radar scale; specifically, inverted roughness differs from LiDAR-derived topography, suggesting the influence of basal snow layer properties. Despite complications arising from spatial heterogeneity of soil properties including freeze/thaw cycles, the results demonstrate that low-frequency retrieval of soil background parameters is a necessary first step for snow applications, but that improved representation of the snowpack remains required to fully exploit higher-frequency observations in temperate environments such as Powassan.

1 Introduction

Snowpack dynamics play an important role in water resources (Zhang, 2005), hydrological processes (Aygün et al., 2020) and ecosystems health (Pulliainen et al., 2020). Despite its importance, snow is one of the few elements of the hydrological cycle that

https://doi.org/10.5194/egusphere-2026-656
Preprint. Discussion started: 22 May 2026

is not monitored from space with sufficient accuracy to meet the needs of operational applications (Derksen et al., 2019). A key property for monitoring snowpack dynamics is the Snow Water Equivalent (SWE), which represents the amount of meltwater contained in a snowpack column (Vionnet et al., 2021; Belinska et al., 2023). Previous studies have demonstrated the potential of radar backscatter measurements for SWE retrieval, especially at Ku-band frequencies (Lemmetyinen et al., 2018; King et al., 2018; Rutter et al., 2019). The ability of Ku-band Synthetic Aperture Radar (SAR) to estimate SWE at local scales arises from the volume scattering of radar signals by snow ice crystals (Lemmetyinen et al., 2022; Tsang et al., 2022; Montpetit et al., 2024). To improve our understanding of these snow/radar interactions and allow SWE retrieval from space, Environment and Climate Change Canada (ECCC) and the Canadian Space Agency (CSA) have developed a satellite mission concept, currently known as the Terrestrial Snow Mass Mission (TSMM) (Derksen et al., 2019; Garnaud et al., 2019). TSMM aims to provide high-resolution annual monitoring of snow conditions globally, with a particular focus on Canada and the Northern Hemisphere. The proposed satellite mission would carry a dual-frequency Ku-band SAR operating at (13.500 ± 0.450) GHz and (17.250 ± 0.450) GHz.

In-addition to snow/radar interactions, the Ku-band radar signal is also influenced by the soil conditions under the snow. To adequately retrieve SWE, the soil contribution must be accounted. Tsang et al. (2022) proposed to model the backscatter contribution of the soil from an optimization of soil parameters (surface roughness and dielectric properties) at low frequencies such as L- or C-band. Then, the inverted soil parameters can be used to estimate the soil backscatter contribution for higher frequencies, such as Ku-band. Similarly, a method for inverting effective soil and snow parameters was recently developed by Montpetit et al. (2024) using multi-frequency airborne and satellite radar data and the Snow Microwave Radiative Transfer (SMRT) model (Picard et al., 2018). To parameterize SMRT, they used SAR data from a field campaign conducted in the winter of 2018/2019 around the Trail Valley Creek (TVC) arctic research station near Inuvik in the Northwestern Territories, Canada. An airborne radar system developed and operated by the University of Massachusetts provided the high frequency Ku-band SAR (13.285 GHz). Additional satellite C- and X-band radar data from the RadarSAT-2 (RSAT-2) and TerraSAR-X (TSX) SAR instruments were also acquired throughout the winter season of the TVC campaign. Their approach consisted of inverting the soil parameters (roughness and permittivity) using the low frequency C- and X-band satellite data, which is less sensitive to volume scattering in shallow, non-alpine snow cover (Duguay and Bernier, 2012; Brangers et al., 2024). The inverted soil parameters were then used in SMRT for the inversion of the snow volume scattering parameter at the Ku-band frequency. Montpetit et al. (2024) successfully applied this method to a tundra environment, showing that by optimizing a single soil roughness parameter and a varying soil permittivity for each radar frequency for different sites, it was possible to accurately reproduce the observed backscatter signal using SMRT at C-, X-, and most importantly at Ku-band. The study from Montpetit et al. (2024) focused on a thoroughly frozen tundra soil, which simplifies the soil dielectric properties and reduces the complexity of the soil-snow interface interactions. Indeed, in higher latitudes such as Inuvik, the subnivian soil tends to be frozen for the majority of the winter season, however such conditions are not representative of more southern snow covered regions. In lower latitudes, the soil beneath the snow cover can exhibit both frozen or thawed states, and can swing back and forth between these states repeatedly during the same winter season (Goodrich, 1982). The changing state of the soil substantially impacts the soil permittivity and how the soil interacts with the radar signal.

https://doi.org/10.5194/egusphere-2026-656
Preprint. Discussion started: 22 May 2026

The current work builds upon the methodology developed by Montpetit et al. (2024) but focuses on an agro-forested site in Powassan, Ontario, which is an example of southern soil and snow conditions compared to the tundra environment of Inuvik. A data collection campaign using Cryospheric SAR (CryoSAR) (Kelly et al., 2024) took place in Powassan, between fall 2022 and winter 2024 with intensive radar surveys conducted during the winter of 2023 (11 flights on different days between October 2022 and April 2023). CryoSAR is a fully polarimetric dual-frequency airborne radar system operating at L-band ((1.3 ± 0.2) GHz) and Ku-band ((13.5 ± 0.6) GHz) with the Ku frequency band similar to the lower projected TSMM band ((13.500 ± 0.450) GHz). Due to the similarity in frequencies, CryoSAR can be used to support TSMM by developing retrieval algorithms for the mission. Coincident to the airborne radar surveys, in situ measurements were recorded, including soil parameters (temperature, permittivity, roughness), snow information (depth, density, grain type, stratigraphy) and meteorological observations (air temperature, relative humidity, wind speed). In addition to CryoSAR airborne SAR data, observations from satellite SAR instruments from Radarsat Constellation Mission (RCM) at 5.405 GHz and TSX at 9.65 GHz were acquired for multiple dates over the winter.

The objective of this study is to evaluate the inversion approach of soil parameters (roughness and permittivity) from Montpetit et al. (2024) using SMRT with the Powassan campaign data, where the soil states were spatially and temporally variable, leading to potential challenges to the inversion approach. The inverted soil parameters are then used to simulate the SAR backscattering signal using SMRT for all available frequencies (L-, C- and X-band) and compared with the observed radar data to evaluate the performance of the model. The inverted soil parameters are also compared with the ground-based measurements collected during the field campaign to assess the accuracy of the inversion approach. The sensitivity of the modelled SAR backscatter for all three instruments with respect to soil parameters was investigated. A one-at-a-time sensitivity analysis is then performed with SMRT across all frequencies up to the CryoSAR and TSMM Ku-bands to characterize how the dominant controls on backscatter shift from soil to snow properties as frequency increases. Finally, the implications of the method in the context of the TSMM SWE retrievals are discussed.

2 Field data acquisition

2.1 Study area

The in-situ measurements and CryoSAR radar surveys were conducted over agricultural land in Powassan, Ontario ($46.08\,^{\circ}$N, $79.34\,^{\circ}$W). The area is characterized by mostly flat fields with small hills on the eastern side. At the time of the study, the snow covered fields were not in use, but in the previous growing season of 2022, some fields were used for pasture, while others were used for crops. Soil analyses show the soil is mostly silt and silt loam with low clay and sand content and organic matter content around $10\,\%$ to $15\,\%$. Zones with permanent soil dielectric probes, soil temperature sensors and snow depth rulers (black squares in Figure 1 (b)) were established prior to snow accumulation. These zones remained undisturbed throughout the winter to ensure accurate soil measurements. Snowpits were dug near these undisturbed zones (red triangles in Figure 1 (b)) as well as at other areas across the study domain to try and measure a wide range of snow conditions. A temporary HOBO U30 weather station (blue diamond in Figure 1 (b)) was also installed in a field to monitor local meteorological conditions

https://doi.org/10.5194/egusphere-2026-656
Preprint. Discussion started: 22 May 2026

throughout the winter season including air temperature, snow depth, wind speed and direction, etc. The first snowfall occurred around mid-November 2022, but a warm spell caused near-complete snowmelt by early December. Permanent snow cover was re-established in mid-December, reaching approximately $18\,\mathrm{cm}$ and increasing steadily to $30\,\mathrm{cm}$ to $45\,\mathrm{cm}$ during the main SAR
90 acquisition period. Mean snow density from snowpit observations was approximately $244\,\mathrm{kg/m^3}$, and the snowpack contained ice lenses and basal ice crusts formed during successive freeze-thaw events. All field visits, airborne surveys, and satellite acquisitions used in this study were conducted during this stable accumulation phase. A detailed account of the seasonal snow and soil evolution is provided in Section 4.1.

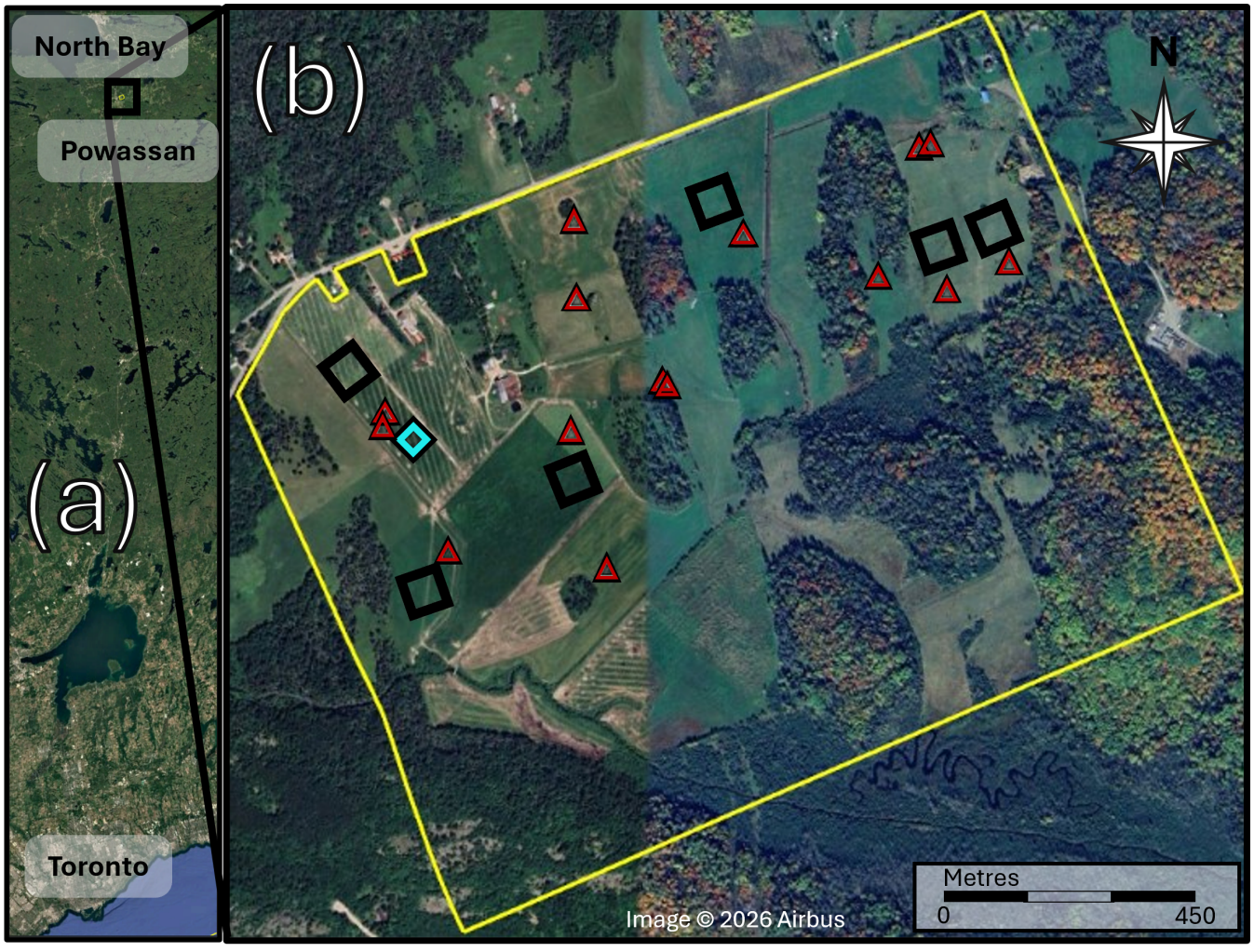

Figure 1. (a) General location of Powassan, the yellow area represents the study area; (b) undisturbed zones (black squares), snowpits (red triangles) and weather station (blue diamond) location

https://doi.org/10.5194/egusphere-2026-656
Preprint. Discussion started: 22 May 2026

2.2 Data acquisition

Multiple site visits were conducted throughout the winter season to collect ground-based measurements, including snow stratigraphy, density, temperature, Specific Surface Area (SSA), and soil permittivity. These measurements were largely coincident with CryoSAR SAR acquisitions, which provided high-resolution ($1\,\mathrm{m} \times 1\,\mathrm{m}$) L-band and Ku-band backscatter data over the study area. Additionally, satellite data from TSX and RCM were acquired (Table 1). While challenging weather and radar equipment problems limited the number of simultaneous measurements, a valuable dataset consisting of 12 satellite and airborne radar observation dates within $\pm$ 1 month of the March 1st field campaign ground observations was acquired.

The dataset includes soil permittivity measurements, crucial for accurate modelling of the underlying surface and key snowpack properties, such as SWE, snow depth, and density, along with corresponding CryoSAR backscatter measurements. The collected data offers a comprehensive dataset that can be used to support radiative transfer models such as SMRT for TSMM algorithms and SWE retrieval approaches.

2.2.1 Ground-based measurements

In Fall 2022, at the beginning of the campaign, six soil monitoring stations were installed, each equipped with two Stevens HydraProbe (HP) sensors (Stevens Water Monitoring Systems, $50\,\mathrm{MHz}$). The locations of these stations (Figure 1 (b)), were selected to capture a range of soil moisture and roughness conditions based on different elevations and land use types. At each soil station, both HP sensors were installed vertically into the soil, measuring soil parameters within the top $0\,\mathrm{cm}$ to $5.7\,\mathrm{cm}$ of the soil. A designated undisturbed area was established around each soil station to maintain pristine snow conditions and prevent interference with the instruments. The values recorded by each HP at each undisturbed site's soil station were averaged together for analysis. These sensors provided continuous measurements of the soil dielectric constant and temperature throughout the winter season at $30\,\mathrm{min}$ intervals.

Snowpits were excavated near these undisturbed zones and other representative locations to provide ground reference measurements. Within each snowpit, detailed observations of snow stratigraphy were recorded, along with vertical profiles of temperature, density, and SSA using either the Infrared Integrating Sphere (IRIS) (Montpetit et al., 2012) or the A2 Photonics IceCube (Gallet et al., 2009). At most of the snowpit sites, Snow Micropenetrometer (SMP) (Proksch et al., 2015) profiles were also gathered near the vertical temperature, density, and SSA profiles and in an area surrounding the snowpits. An Open-Ended Coaxial Probe (OECP) able to measure the dielectric properties of a material from $1\,\mathrm{GHz}$ to $18\,\mathrm{GHz}$ was also used to measure the soil permittivity (Gélinas et al., 2025) during the March 1st campaign.

2.2.2 Remote-sensing data

The CryoSAR instrument, a dual-frequency quad-polarization (HH, HV, VH, VV) SAR operating at $(1.3 \pm 0.2)\,\mathrm{GHz}$ and $(13.5 \pm 0.6)\,\mathrm{GHz}$, is a modular system adaptable to various aircraft platforms. The instrument was mounted on a Cessna 208B Grand Caravan. The system is capable of making polarimetric backscatter measurements with a ground range resolution of $1\,\mathrm{m} \times 1\,\mathrm{m}$ in range and azimuth at an altitude of $1500\,\mathrm{m}$. The noise floor for the L-band instrument is approximately $-28\,\mathrm{dB}$.

https://doi.org/10.5194/egusphere-2026-656
Preprint. Discussion started: 22 May 2026

In-field L-band and Ku-band corner reflectors were positioned for backscatter calibration. Figure 2 illustrates the flight paths followed during the multiple CryoSAR radar surveys. Track 4 was used for the SAR acquisition data since this track is optimal for the L-band corner reflector target. In addition to the CryoSAR data, satellite SAR data from TSX and RCM was used.

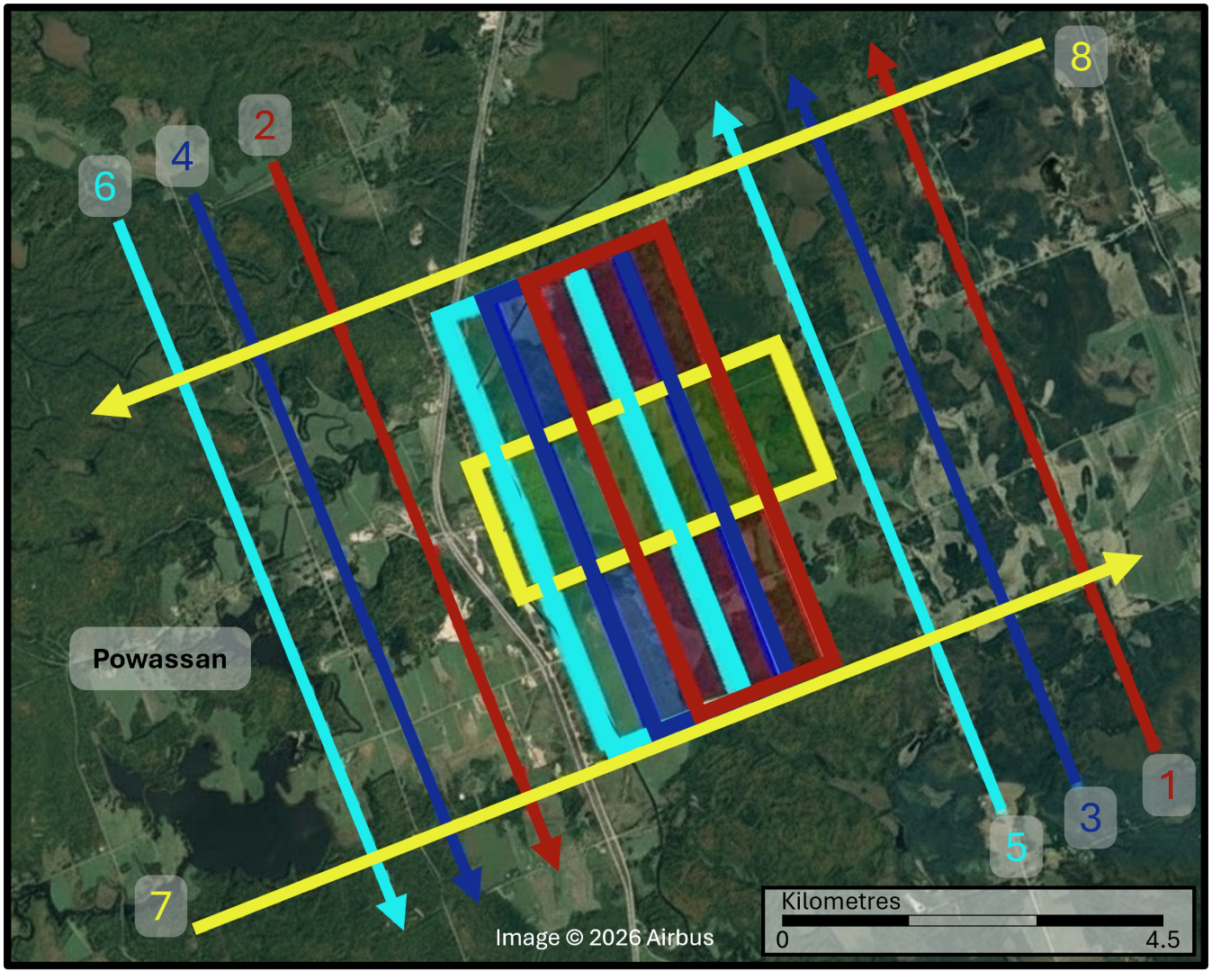

Figure 2. Flight paths and swath coverage of the airborne SAR over the studied area. The same lines were kept for all the surveys.

Before the first snowfall of the season, bare-ground drone-based LiDAR surveys were conducted to produce a high resolution digital elevation model, to establish a baseline for subsequent snow depth mapping, and to characterize soil surface roughness. A DJI Matrice 210 V2 drone was equipped with Green Valley International's LiAir V LiDAR (LIVOX mid-40) operating at a wavelength of $905\,\mathrm{nm}$ with a field of view of $38.4°$. The drone flew at an altitude of $30\,\mathrm{m}$ over $80\,\mathrm{m} \times 80\,\mathrm{m}$ zones centered on each snowpit, for a total point density of $1400\,\mathrm{pts/m^2}$.

https://doi.org/10.5194/egusphere-2026-656
Preprint. Discussion started: 22 May 2026

Table 1. Radar frequencies and acquisition dates used in this study. The TSMM rows are projected mission bands and therefore have no acquisition dates.

Sensor	Center Freq.	Bandwidth	Acquisition dates (2023) / usage
CryoSAR-L	1.3 GHz	0.2 GHz	Mar 01, Mar 03, Mar 15, Mar 30
RCM-C	5.405 GHz	0.1 GHz	Feb 16, Feb 22, Mar 02, Mar 10, Mar 16
TSX-X	9.65 GHz	0.3 GHz	Feb 20, Feb 28, Mar 03
CryoSAR-Ku	13.5 GHz	0.6 GHz	
TSMM-Ku1	13.5 GHz	0.450 GHz	Snow sensitivity only
TSMM-Ku2	17.25 GHz	0.450 GHz	

3 Data processing and modelling

This section describes the processing steps required to prepare all of the field data for input into SMRT: including the SAR signal processing and calibration, the snow measurements and the soil parameters. Then, the modelling algorithm used to invert the soil parameters and a sensitivity analysis of the soil conditions are explained.

3.1 SAR data processing

Processing of the airborne SAR data was done using MetaSAR Pro software which focuses each acquisition track and geometrically and radiometerically corrects the SAR data. The L-band corner reflector was mid-swath and provided a suitable target to calibrate the data to within about 1 dB absolute calibration accuracy. As part of this processing chain, the radar signal was corrected for local incidence angle using available High Resolution Digital Elevation Model (HRDEM) (NRCan, 2025) and multi-looked to reduce the impact of speckle noise. A spatial average of $20\,\mathrm{m} \times 20\,\mathrm{m}$ centered around each snowpit location for all instruments (CryoSAR, RCM, and TSX) and all dates (see Table 1) was applied to link the SAR observations to ground measurements. The averaging area size was chosen to balance spatial representativeness and minimize land cover heterogeneity effects within the undisturbed areas. This step ensured that the SAR backscatter values for each sensor were at the same scale to compare with the simulated values from SMRT.

3.2 Snow and soil data processing

The field visit on March 1st, 2023, provided the most comprehensive field measurement dataset with simultaneous CryoSAR acquisitions. The snowpit measurements recorded from this date were used as input for the snow representation during the modelling steps for all 12 SAR observation dates, because they included all of the necessary snow information needed (layer thickness, density, temperature and SSA).

https://doi.org/10.5194/egusphere-2026-656
Preprint. Discussion started: 22 May 2026

3.2.1 Snowpack measurements

Due to the variable temperature and weather of the 2023 winter season, a complex snowpack developed with multiple ice lenses and a substantial ice crust at the bottom layer for some locations within the study domain. For the purpose of this study, the number of layers were aggregated in the snowpack by grain type and averaged to reduce the number of similar layers while preserving the overall snowpack structure.

3.2.2 Soil properties

For comparison purposes, the seasonal evolution of soil permittivity from the HP sensors were averaged for the two sensors at each undisturbed site. This spatial average was then used to extract the daily average on March 1st, 2023, for comparison purposes. In addition, the soil dielectric properties were also measured with the OECP during the snowpit excavations on March 1st, 2023. For each snowpit, the underlying soil was measured at least 5 times in a $3\,\mathrm{m} \times 3\,\mathrm{m}$ area and averaged to account for soil heterogeneity. Since the coaxial probe measures a continuous spectrum from $1\,\mathrm{GHz}$ to $18\,\mathrm{GHz}$, an average over the frequency ranges summarized in Table 1 was extracted to compare with the inverted soil parameters.

For each snowpit location, the soil roughness parameters, Root Mean Squared Height (RMSH) and Correlation Length (l_c), were extracted from the LiDAR point cloud acquired on November 15, 2022 before snowfall. A $20\,\mathrm{m} \times 20\,\mathrm{m}$ subset of the lidar point cloud was extracted for each area of interest. The roughness parameters were then calculated using a plug-in tool named Roughness from Point Cloud Profiles (Chabot et al., 2018). This tool is available in Whitebox Geospatial Analysis Tools (GAT) software version 3.4.0 (Lindsay, 2016). The tool was run in azimuth mode at 7.5 degree increments, and functions by sampling point elevations along a series of profiles drawn across the $20\,\mathrm{m} \times 20\,\mathrm{m}$ LiDAR point cloud subset. Each profile was $20\,\mathrm{m}$ in length, spaced a part by $0.5\,\mathrm{m}$, and sampled at $0.01\,\mathrm{m}$ producing a distribution of roughness metrics based on azimuth for each area of interest. The mean RMSH and minimum l_c for each area of interest were then calculated and used to compute the mean square slope $(\mathrm{MSS})_{\mathrm{LiDAR}}$ (Eq. 1).

$$\mathrm{MSS}_{\mathrm{LiDAR}} = 2\left[\frac{\mathrm{RMSH}}{l_c}\right]^2 \tag{1}$$

3.3 Modeling with SMRT

For the SMRT simulations, the electromagnetic model used was Improved Born Approximation (IBA) (Mätzler and Wiesmann, 1999), alongside the Discrete Ordinate and Eigenvalue Solver (DORT) radiative transfer solver (Picard et al., 2004, 2013). The snow microstructure was represented by an exponential autocorrelation function model, and the soil scattering model used the geometrical optics approximation with static complex permittivity to be optimized.

3.3.1 Inversion model

The soil parameter inversion was performed using a least-squares minimization approach to minimize the cost function J (Eq. 2) defined as the sum of the squared differences between the observed σ^0_{obs} and simulated σ^0_{sim} for the different radar

https://doi.org/10.5194/egusphere-2026-656
Preprint. Discussion started: 22 May 2026

frequencies available for each date per site. This approach led to the optimization of one MSS per site for the entire winter, and the permittivity (real and imaginary parts) per date/frequency. The optimization's initial values x_0 were set to: mss $= 0.01$, $\varepsilon' = 12$, and $\varepsilon'' = 5$ and were identical for all sites and dates. The least-squares approach allowed the algorithm to set boundaries for the inversion parameters: mss $\in [0.001, 1]$, $\varepsilon' \in [2, 58]$, and $\varepsilon'' \in [0.1, 25]$. The boundaries for the permittivity values were chosen based on the literature (Dobson et al., 1985; Bircher et al., 2016; Gélinas et al., 2025), from completely dry or frozen values to nearly over saturated soil conditions. The values for the MSS boundaries were selected to cover a wide range of possible soil roughness conditions, leaving a large margin for the parameter optimization (see Section 5.3).

$$J = \sum_{i=1}^{N} \left(\sigma^0_{\text{obs},i} - \sigma^0_{\text{sim},i}\right)^2 \tag{2}$$

During the optimization process, it was observed that for some sites, the cost function could be minimized by varying only the soil roughness parameter while keeping the soil permittivity close to the initial guess values. To prevent this behavior and ensure a realistic inversion of the soil parameters, a penalty term based on the Tikhonov method was added to the cost function for the permittivity parameters (Eq. 3). This penalty term allowed the algorithm to avoid biasing the optimization towards only one of the parameters by adding a small cost for solutions deviating from the initial guess values.

$$\begin{aligned} J = \sum_{i=1}^{N} \Big\{ & \left(\sigma^0_{\text{obs},i} - \sigma^0_{\text{sim},i}\right)^2 \\ & + \lambda \left[\left(\varepsilon'_i - \varepsilon'_{0,i}\right)^2 + \left(\varepsilon''_i - \varepsilon''_{0,i}\right)^2 \right] \Big\} \end{aligned} \tag{3}$$

where λ is the regularization parameter set to 1×10^{-4} to give the optimization more confidence in the observed data rather than the initial guess values, and $N = 12$ is the number of observation dates.

3.3.2 Sensitivity analysis

To test the sensitivity of the radar backscatter to the soil parameters, a sensitivity analysis was performed using the SALib library (Herman and Usher, 2017; Iwanaga et al., 2022). The analysis was based on the Sobol method (Sobol', 2001), which is a variance-based sensitivity analysis technique that quantifies the contribution of each input parameter to the output variance. For this analysis, the input parameters were the soil roughness (MSS) and soil permittivity (real and imaginary parts), and the output was the simulated backscatter coefficient (σ^0) from SMRT in HH and VV polarizations. Instead of using all inverted soil parameters as input for the sensitivity analysis, the problem was simplified by studying the effect of applying a scaling factor to the MSS, and two scaling factors to all inverted ε', and ε'' values per site. The scaling factor for MSS varied between 0.5 to 1.5, while the scaling factors for ε' and ε'' varied between 0.75 to 1.25. Since the inverted soil permittivity values already varied for each date and frequency, applying a scaling factor allowed to study the overall sensitivity of the backscatter to changes in soil permittivity without increasing the dimensionality of the problem.

A grid type sensitivity analysis was also performed to visualize the effect of changing the soil parameters on the backscatter values using an average snowpack from the Powassan dataset. For this analysis, the MSS was varied between 0.03 to 0.3 with

https://doi.org/10.5194/egusphere-2026-656
Preprint. Discussion started: 22 May 2026

0.015 size steps, while ε' was varied between 2 to 60 with 2 and ε'' was set to 8. The backscatter values were then simulated for all combinations of the three parameters, using SMRT for both HH and VV polarizations. Since the geometrical optics approximation used in SMRT depends on the frequency only indirectly through the permittivity, no frequency variation was applied for this analysis.

A one-at-a-time experiment was conducted using a single-layer snowpack parameterized from the Powassan snowpit observations, varying one parameter at a time from L- to Ku-band while holding all others at their baseline values. Two contrasting soil states, representing frozen and unfrozen/wet conditions, were used to bracket the range of soil backgrounds encountered at the site. The swept parameters included soil permittivity, soil roughness, snow density, snow depth, and the exponential correlation length of the snow microstructure. Baseline values for the snow parameters were set to the means observed in the Powassan snowpits: $\rho = 244\,\mathrm{kg/m^3}$, $p_{ex} = 0.21\,\mathrm{mm}$, and snow depth of $0.34\,\mathrm{m}$. The upper bound of the exponential correlation length sweep was set to $0.70\,\mathrm{mm}$ — just above the maximum value observed in the Powassan snowpits ($0.58\,\mathrm{mm}$) — to remain within the validity domain of the IBA formulation at $\mathrm{Ku_2}$. Beyond this threshold, the single-scattering albedo predicted by IBA becomes unphysical at $17.25\,\mathrm{GHz}$, indicating that the largest grain sizes observed in these temperate snow conditions already approach the upper limit of the perturbative scattering regime at this frequency (Picard et al., 2022).

4 Results

4.1 Meteorological analysis

Figure 3 presents the time series of the different permanently installed meteorological and soil monitoring sensors in the Powassan fields throughout the winter season. It is important to note that a frozen soil generally exhibits a significantly lower real permittivity (typically between 2 and 4) compared to a thawed soil (which can range from 10 to over 30 depending on moisture content) (Mironov et al., 2010). The first permanent snowfall occurred around mid-November 2022, accompanied by a gradual decrease in air and soil temperatures, as registered by both the weather station and the HP. Afterwards, a warm spell occurred at the end of November and early December, causing a significant snowmelt event and multiple freeze-thaw cycles in the soil. According to the HP measurements, the soil experienced a first frozen period for about one week during the second week of December, where the average soil real permittivity dropped to values below 10 for the first time (representing frozen soil conditions). This decrease in soil permittivity coincides with the air temperature dropping below freezing, along with gradual snow accumulation of approximately $18\,\mathrm{cm}$, as indicated by the automated snow depth measurements from the local weather station. This resulted in a frozen, snow-covered soil condition persisting until the end of December. This frozen period was followed by another warm spell in early January, causing the soil to thaw. Colder weather returned in mid-January, with increasing snow accumulating and the soil entering a two week period of freeze/thaw cycles. By the end of January, the snow reached a depth of approximately 40cm and its insulating properties muted the impact of consistently colder air temperatures on the soil, leading to persistent soil temperatures around $0\,^\circ\mathrm{C}$. However, as the soil temperature remained constant around the freezing point, the soil permittivity kept fluctuating between frozen and thawed conditions until mid-February before eventually stabilizing into a state where the real permittivity showed values strictly above 10 (thawed) for the remainder of the winter

https://doi.org/10.5194/egusphere-2026-656
Preprint. Discussion started: 22 May 2026

245 season. The soil conditions coinciding with the SAR acquisition dates (see Table 1) and the March 1st field survey date were in a mixed state, where some undisturbed sites were partially frozen and others partially unfrozen and wet or dry. These observations and measurements highlight the complex and dynamic nature of the thermal and dielectric properties of the soil during the

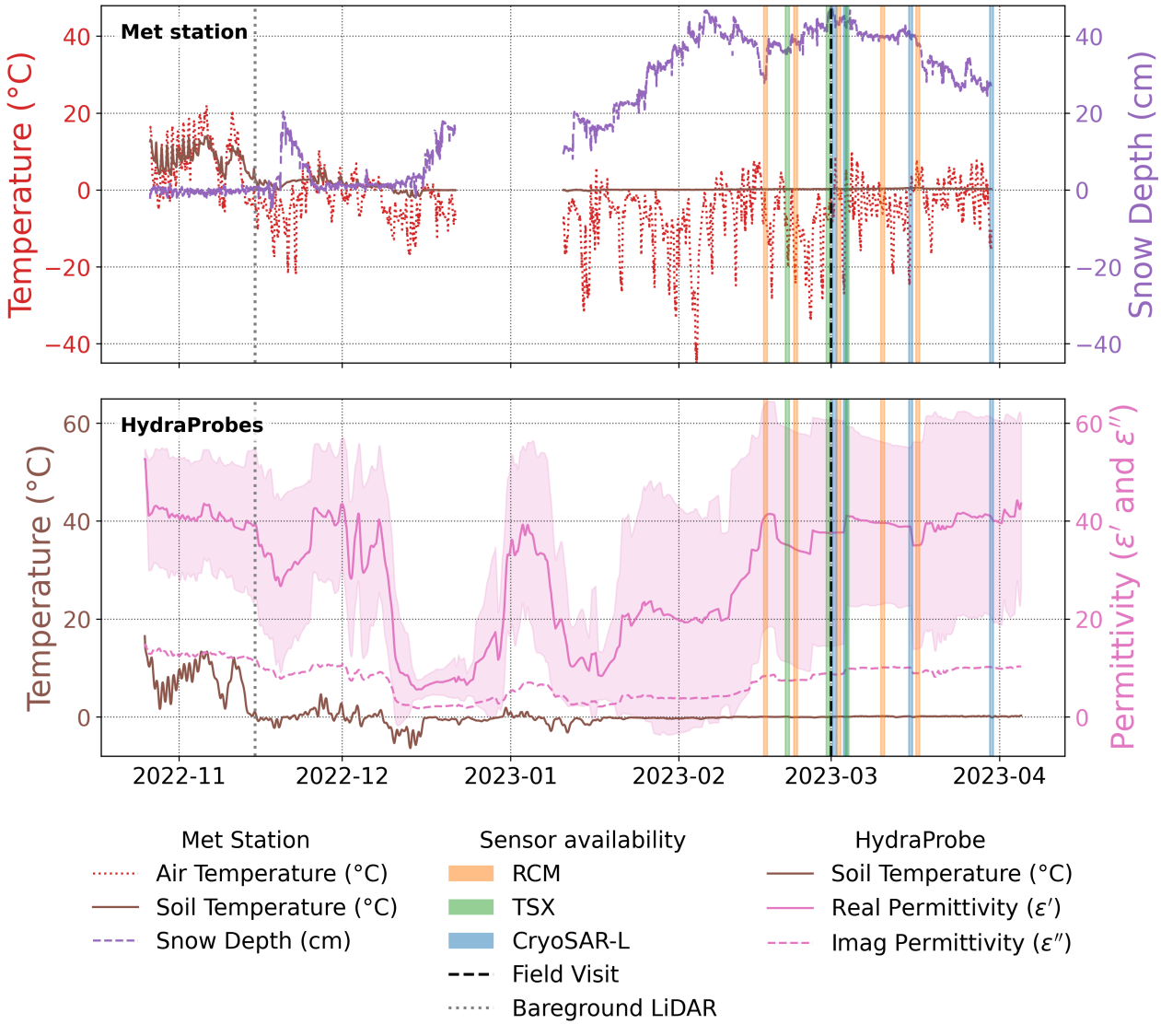

Figure 3. The top graph shows soil and air temperatures with snow depth, recorded by the weather station throughout the season. The airborne and spaceborne acquisition dates are highlighted with colored bars; the field-visit and bareground LiDAR date are also shown. The gap in the met station time series was due to a power loss, but it did not coincide with any site visits. The bottom graph shows the average real and imaginary soil permittivity and temperature measured by the Stevens HP for all probes at all sites. The shading around the real permittivity represents one standard deviation above and below the average value.

https://doi.org/10.5194/egusphere-2026-656
Preprint. Discussion started: 22 May 2026

winter season, providing the unique opportunity to both run and evaluate a model-based inversion approach to estimate effective soil parameters at the scale of the radar observations. These thermal and dielectric soil properties are crucial for understanding the interactions between the radar backscattering signal and the snowpack when trying to retrieve SWE.

4.2 Soil microwave properties inversion

The optimization was performed one site at a time using all available frequencies (CryoSAR, RCM, and TSX), resulting in inverting a single soil roughness MSS value per site for the entire winter alongside a time-varying soil permittivity for the 12 SAR acquisition dates. Figure 3 shows that the snow accumulation remained relatively stable throughout the SAR acquisition dates, with snow depth ranging from 30 cm to 45 cm, which further supports the choice to use the March 1st snow survey observations to represent the snowpack in SMRT for all SAR measurements. Figure 4 shows the comparison between the different SAR platform radar-observed backscattering and forward simulated backscattering coefficients after the inversion of soil parameters.

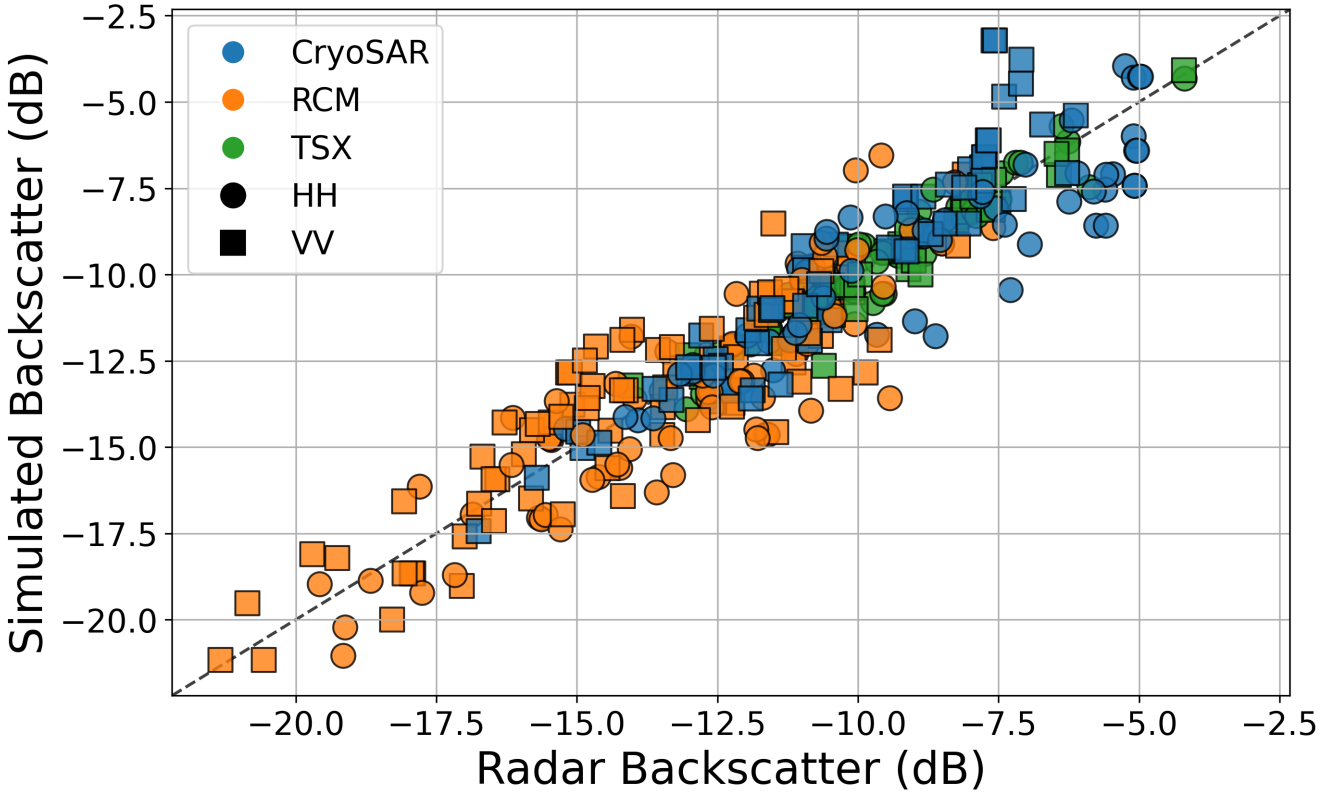

Figure 4. Comparison between simulated and observed SAR backscatter for all sensors at all dates and sites for both polarizations

Table 2 summarizes the statistics of the optimization results for each radar system and polarization.

https://doi.org/10.5194/egusphere-2026-656
Preprint. Discussion started: 22 May 2026

Table 2. Optimization statistics for Figure 4; column *General* computes the statistics for all three sensors; row **All** computes the statistics for both polarization; the cell for **All**/*General* represent the global statistics. RMSE and bias are in dB.

	General	CryoSAR	RCM	TSX
VV	R^2 (0.88)	0.84	0.77	0.92
	RMSE (1.23)	1.32	1.43	0.57
	Bias (-0.20)	-0.46	-0.17	0.12
HH	R^2 (0.85)	0.74	0.76	0.92
	RMSE (1.28)	1.34	1.52	0.56
	Bias (0.33)	0.44	0.44	0.01
All	R^2 (0.87)	0.81	0.77	0.92
	RMSE (1.25)	1.33	1.47	0.56
	Bias (0.07)	-0.01	0.13	0.06

Generally, the optimization showed results with R^2 values above 0.74 and RMSE values below $1.52\,\mathrm{dB}$ for all radars and polarizations. These results show that the forward model reproduced the observed backscatter with good accuracy after inverting both soil parameters (roughness and permittivity). The bias values are also relatively low, indicating that there is no significant systematic error in the optimization. Additionally, limiting the optimization to a single soil roughness MSS per site for the whole winter season prevented overfitting the data and ensured that the resulting optimized soil parameters remained physically meaningful. Indeed, giving the inversion algorithm too much freedom by inverting one MSS per site, per date yielded poorer results than the more constrained method used.

4.3 Comparison with field data

Figure 5 presents the comparison between the inverted soil permittivity from the optimization and the field measurements from both the HP and the OECP. A first noteworthy observation is that the measured permittivity values show a strong variation between sites due to the heterogeneous soil, terrain, elevation conditions found within the study area. The inverted permittivity values follow the expected trends of decreasing with increasing frequency which also fits with the field measurement trend. However, the inverted permittivity values tend to be lower than the OECP measurements, with less variability noted between undisturbed sites.

Figure 6 shows the comparison between the inverted soil roughness $\mathrm{MSS_{inv}}$ from the optimization and the $\mathrm{MSS_{LiDAR}}$ calculated from the LiDAR data acquired before snowfall for March 1st snowpit survey sites. It should be noted that the $\mathrm{MSS_{LiDAR}}$ values use the average RMSH and minimum l_c over the $20\,\mathrm{m} \times 20\,\mathrm{m}$ area centered on each snowpit. Considering the average l_c instead of the minimum would lead to much lower MSS values, and the LiDAR roughness values would be orders of magnitude lower than the inverted values. Figure 6 also includes coloration based on the snowpack bottom layer density measured in the snowpit during the March 1st survey campaign, as well as the grain type of the bottom layer. The four sites with the highest inversion error showed the presence of an ice crust at the snow-soil interface, and among these, the site with the most error exhibited a very dense bottom layer ($440\,\mathrm{kg/m^3}$). It is also important to note that sites with Crust/Ice bottom layer type with the smaller

https://doi.org/10.5194/egusphere-2026-656
Preprint. Discussion started: 22 May 2026

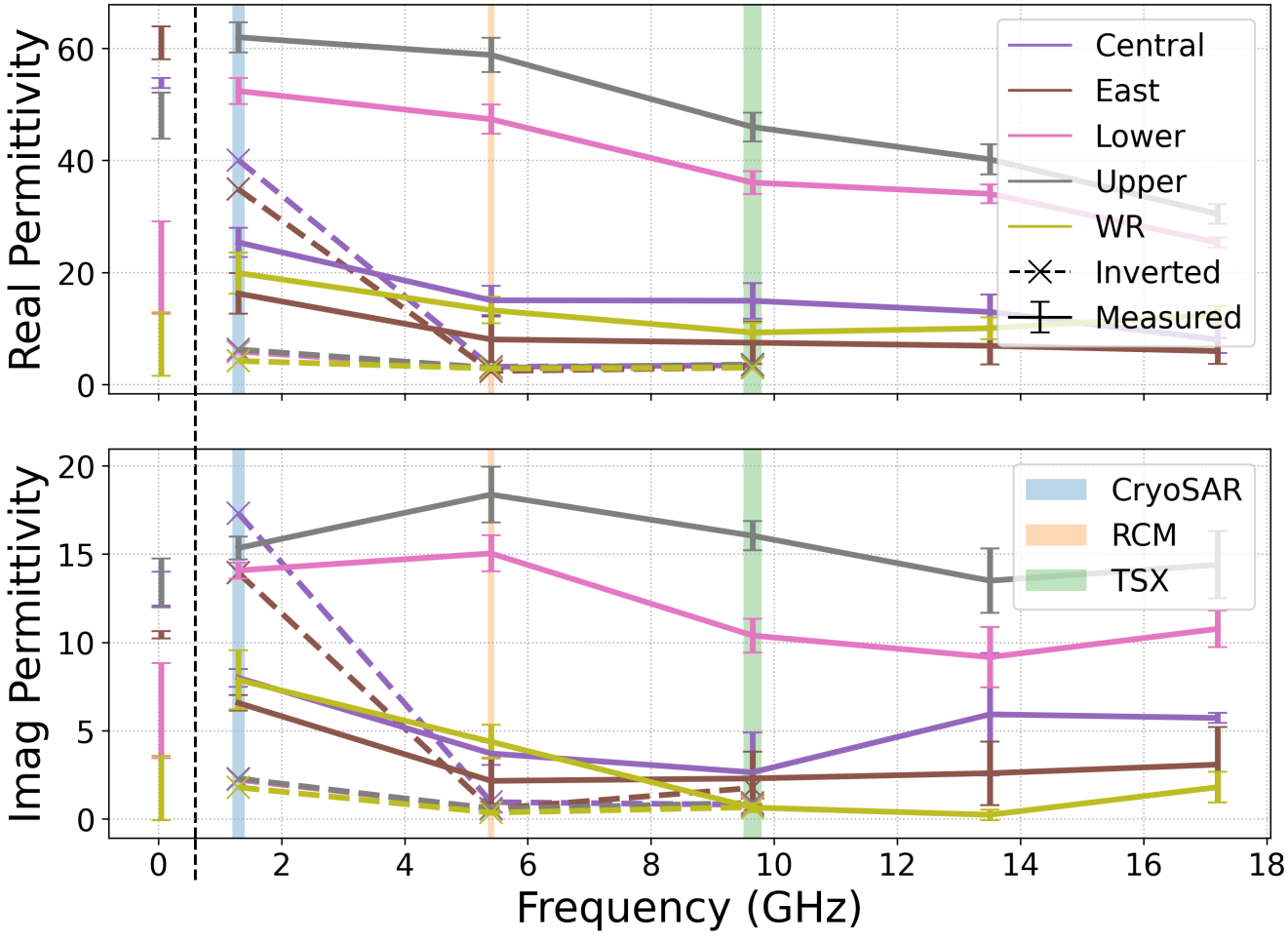

Figure 5. Comparison of inverted permittivity results with in situ measurements from the HP (50 MHz, left of the black dashed line) and the OECP (1 GHz to 18 GHz, right of the black dashed line)

densities (below 300 $\mathrm{kg/m^3}$) are likely due to measurement limitations, where either the bottom crust layer was too thin for accurate measurement and inadvertently included other grain types, or the sampled crust was interlaced with grass, vegetation, and pores, resulting in underestimated density values. These thinner layers also have inverted MSS values closer to the LiDAR measured roughness, which further supports the idea that the presence of a thicker crust at the bottom of the snowpack can influence the SAR backscatter.

4.4 Sensitivity analysis

Figure 7 presents the results of the Sobol sensitivity analysis for the three soil parameters ($\mathrm{MSS_{inv}}$, ε', and ε'') at the three radar frequencies (C-, L-, and X-bands) and both polarizations (HH and VV). The Sobol indices shown in the heatmap represent the

https://doi.org/10.5194/egusphere-2026-656
Preprint. Discussion started: 22 May 2026

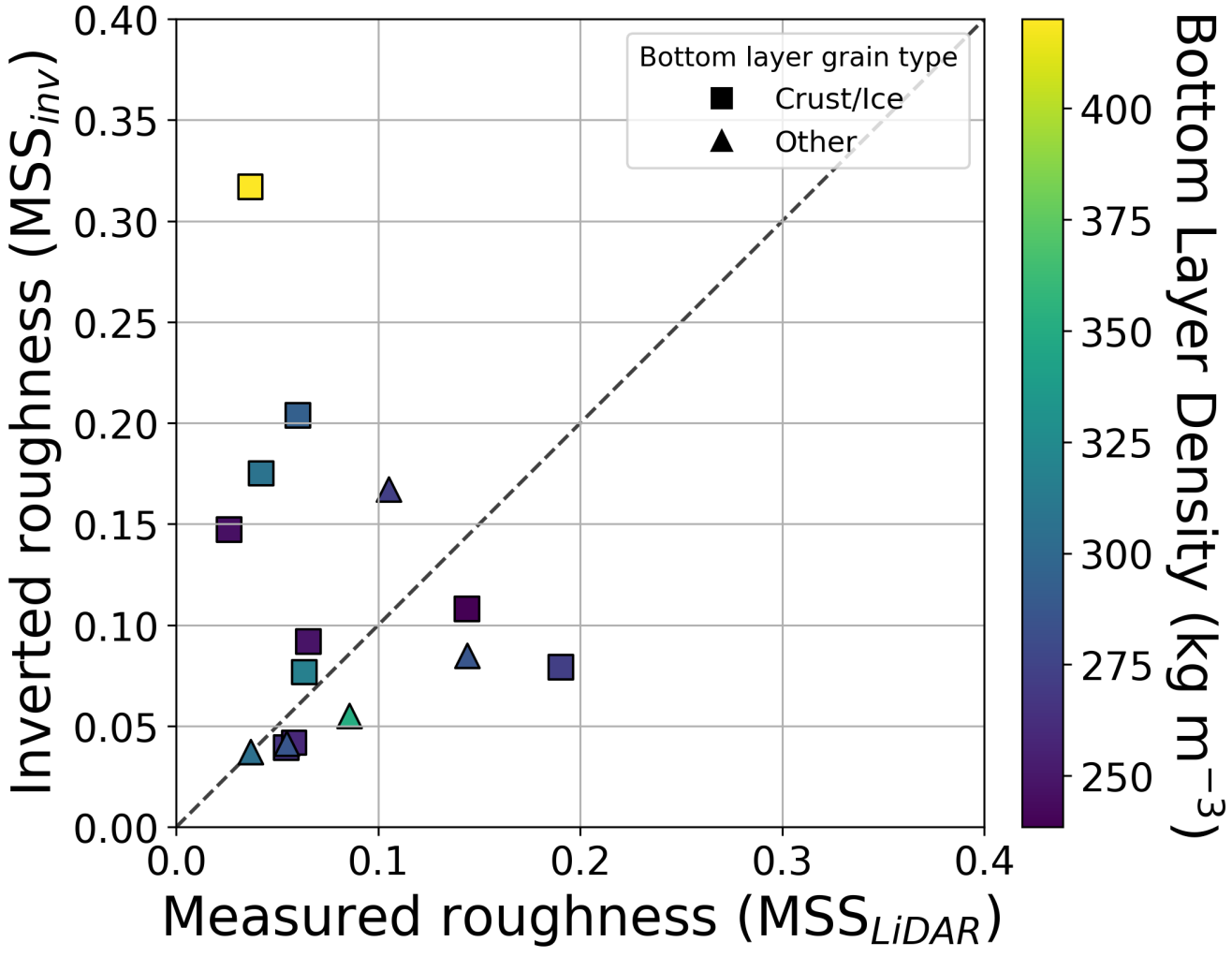

Figure 6. Comparison of inverted roughness with field data from pre-snow LiDAR surveys for selected sites colored by snowpack bottom layer density, highlighting the nature of the bottom layer.

https://doi.org/10.5194/egusphere-2026-656
Preprint. Discussion started: 22 May 2026

total effect of each parameter on the backscattering coefficient, with higher values indicating a greater influence. The total Sobol index for each parameter is calculated by summing the first-order and higher-order effects, providing a comprehensive measure of each parameter's contribution to the variability in the backscattering signal. The analysis reveals that the soil roughness

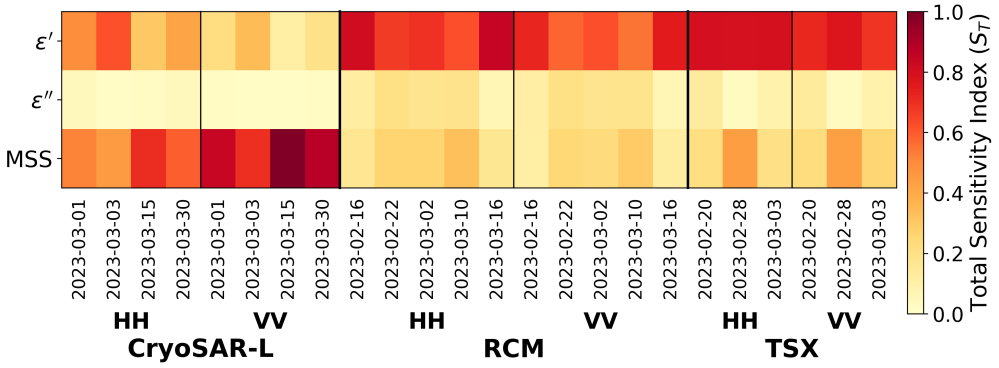

Figure 7. Sobol sensitivity analysis heatmap for soil parameters for the different SAR platforms and two polarizations measured in this study

MSS_{inv} has the highest influence on the backscattering coefficient for the CryoSAR L-band SAR, particularly in VV polarization. For the RCM and TSX, the real part of the soil permittivity (ε') has a more significant impact on the backscattering, with slightly more influence on the HH polarization. The imaginary part of the soil permittivity (ε'') shows a relatively low influence across all frequencies and polarizations.

Figure 8 shows the results of the grid type sensitivity analysis. Here the imaginary part of the soil permittivity (ε'') was held constant at a value of 8 while varying the real part of the soil permittivity (ε') and the soil roughness MSS_{inv} across a slightly extended range between the minimum and maximum inverted values ($MSS_{inv} \in [0.03, 0.3]$ and $\varepsilon' \in [2, 60]$). The heatmaps illustrate how changes in these two parameters affect the backscattering coefficient simulated by SMRT for HH and VV polarizations. The vertical colored lines drawn on the top and bottom axes in Figure 8 for each SAR platform show the maximum permittivity values obtained from the inversion for each radar frequency. This means that the area to the left of each line represents the range of soil parameters that were explored during the inversion for each radar system, with $\varepsilon' \in [2, \sim 5]$ representing a frozen soil state. In general, both polarizations exhibit similar trends, with the backscattering coefficients increasing with higher soil roughness and permittivity values. However, VV polarization shows a more pronounced sensitivity to changes in soil roughness, particularly for low permittivity values (frozen or dry soil conditions) compared to HH polarization. For a given permittivity higher than 20, the backscatter shows lower values for the VV polarization for roughness values below 0.12, hence the VV configuration at the permittivity values available to the L-band sensor shows a greater sensibility to the roughness values.

The one-at-a-time sensitivity analysis was used to evaluate how the relative contribution of the soil and snow evolves from L- to Ku-band (Figure 9). In this diagnostic experiment, a simplified single-layer snowpack was constructed using baseline values derived from the Powassan snowpit measurements ($\rho = 244\,\mathrm{kg/m^3}$, $p_{ex} = 0.21\,\mathrm{mm}$, depth $= 0.34\,\mathrm{m}$, MSS $= 0.1$), and

https://doi.org/10.5194/egusphere-2026-656
Preprint. Discussion started: 22 May 2026

each parameter was varied independently while all others were held fixed. Two contrasting soil states were considered: a frozen soil ($\varepsilon' = 3$, $\varepsilon'' = 0.5$) and an unfrozen wet soil ($\varepsilon' = 15$, $\varepsilon'' = 5$). The simulated response at low frequencies remains strongly controlled by the soil parameters. Under frozen conditions, the real part of the soil permittivity produces the largest variations in simulated backscatter across the frequency range and its dynamic range still decreases toward Ku-band. The MSS response is also strong at L- and C-band, but weakens at the highest frequencies. Under unfrozen wet soil conditions, the response is dominated by MSS at all frequencies, with soil permittivity showing comparatively little variation.

Among the snow parameters, the exponential correlation length shows the clearest frequency-dependent increase in sensitivity. Its response is nearly flat at L- and C-band. It becomes visible from X-band and reaches its largest amplitude at Ku_1 and Ku_2, especially for frozen soil. Snow depth follows the same tendency but with a weaker amplitude, mainly under frozen conditions. Snow density behaves differently. Increasing density monotonically decreases simulated backscatter under frozen conditions at all frequencies. The largest variations occur at L- and C-band, and the effect weakens toward Ku-band. Under unfrozen conditions, the density response is small and weakly decreasing relative to the MSS response (Figure 9).

The transition is also visible in the frequency-parameter response surfaces for frozen and unfrozen soil cases (Figure 10). Large differences between the frozen and unfrozen panels indicate that the soil state remains an important control on the simulated backscatter. Where the two panels become more similar, the response is less dependent on the soil background. This occurs most clearly for p_{ex} toward Ku-band. Snow depth shows a weaker Ku-band increase, while soil permittivity and MSS retain the strongest contrasts between soil states at lower frequencies.

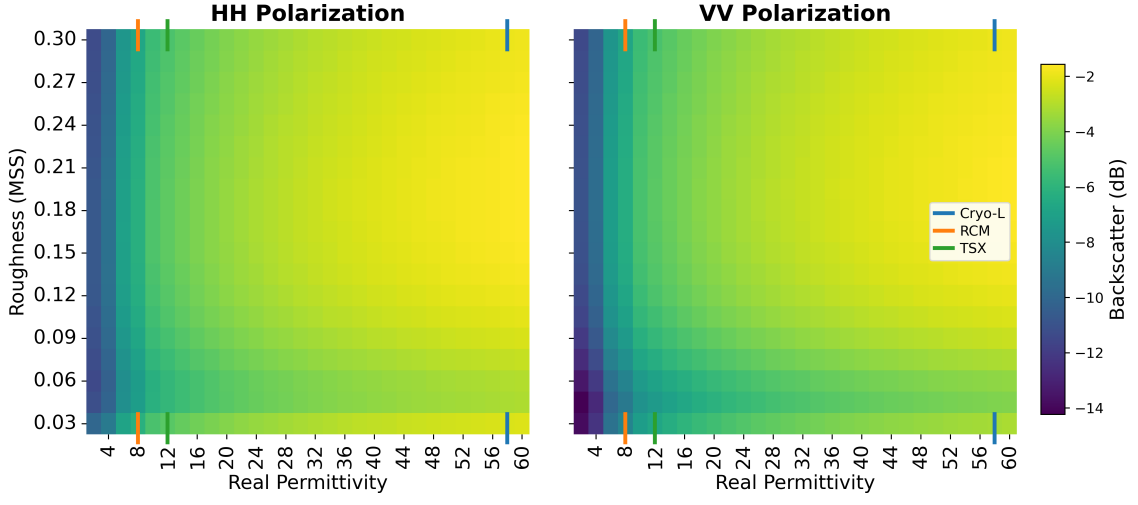

Figure 8. Heatmap of backscattering coefficient sensitivity for a sensitivity analysis of SMRT to soil parameters for an average snowpack from the 2023 Powassan campaign

https://doi.org/10.5194/egusphere-2026-656
Preprint. Discussion started: 22 May 2026

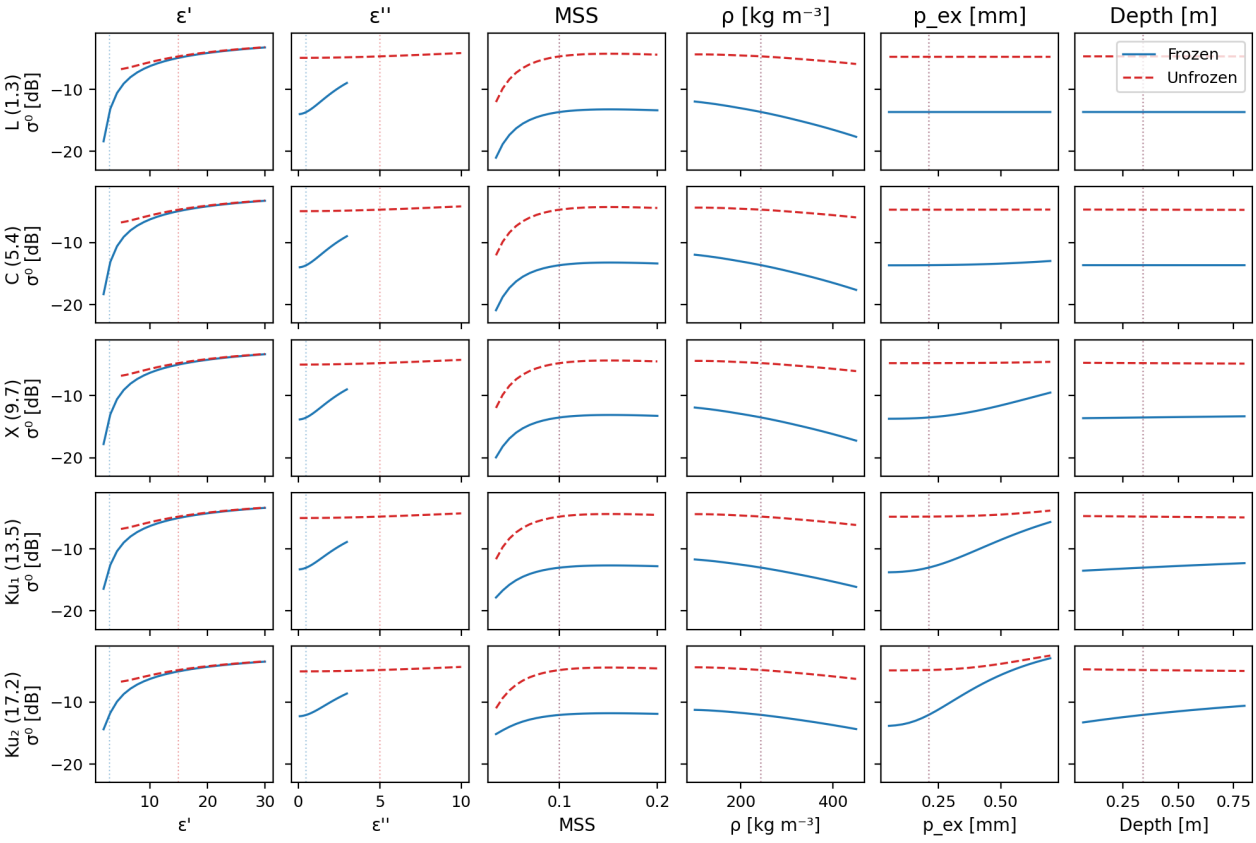

Figure 9. One-at-a-time sensitivity of simulated backscatter to soil and snow parameters from L- to Ku-band. Curves are shown for frozen and unfrozen soil states using a single-layer Powassan snowpack with all non-varied parameters held at baseline values (dotted vertical lines).

5 Discussion

5.1 Powassan study

The field campaign conducted in Powassan during the winter of 2022/2023 provided the opportunity to collect a comprehensive dataset of in-situ and remote sensing soil and snow measurements over a temperate snow-covered agricultural area. Compared to Montpetit et al. (2024)'s winter campaign of 2018/2019 in a tundra environment, this study offers more variable dielectric soil conditions. The fact that local soil conditions varied both spatially and in time during this study offers the unique opportunity to test the robustness of inverting effective soil parameters under a snow cover, using lower frequency SAR measurements.

5.2 Effective dielectric constant

This study highlights the on-going challenge of assessing the soil state using both airborne and space-based measurements and validating them with in-situ point-based ground observations, (OECP and HP), due to issues of scale (see Figure 5). The HP

https://doi.org/10.5194/egusphere-2026-656
Preprint. Discussion started: 22 May 2026

Table 3. Penetration depth values estimation for frozen ($\varepsilon = 2.5 - 0.5i$) and unfrozen moist ($\varepsilon = 30 - 10i$) soil conditions for the SAR systems used in this study.

Frequency	Penetration Depth (cm)	
(GHz)	Frozen	Unfrozen
1.3 (CryoSAR)	11.9	2.1
5.405 (RCM)	2.8	0.5
9.65 (TSX)	1.6	0.3

stations, although they were placed at different representative locations within the study area, did not necessarily represent the fine spatial horizontal heterogeneity of the soil conditions. Another aspect is the range in vertical variability of soil properties within the soil column, which might not be captured by the HP measurements that provide a single integrated measurement of soil moisture and temperature within the top $0\,\mathrm{cm}$ to $5.7\,\mathrm{cm}$ of the soil. On the other hand, the OECP allowed measuring the horizontal spatial heterogeneity of the soil surface within the snowpit footprint by acquiring multiple measurements, but the $3\,\mathrm{m} \times 3\,\mathrm{m}$ snowpit footprint might still not have been representative of the $20\,\mathrm{m} \times 20\,\mathrm{m}$ footprint of the airborne/spaceborne scales. Also, the fact that the OECP only acquires measurements at the very surface of the soil ($0.5\,\mathrm{cm}$ to $0.75\,\mathrm{cm}$ for a dry medium and $\sim 0.3\,\mathrm{cm}$ for a water saturated medium (Gélinas et al., 2025)) can lead to discrepancies when trying to compare with the retrieved soil parameters by low-frequency microwave remote sensors due to the deeper soil penetration depths of these SAR platform instruments. Indeed, the signal penetration depth for microwave SAR can be approximated (Ulaby et al., 1982).

Table 3 shows penetration depth values for typical soil dielectric properties observed during the field campaign at the different radar frequencies used in this study with values ranging from approximately $0.3\,\mathrm{cm}$ to $12\,\mathrm{cm}$ depending on the soil conditions and radar frequency. Another factor in the discrepancies observed between the inverted permittivity values and the ground-based measurements could be the presence of measurement artifacts, such as multi-moding effects in the OECP measurements, which

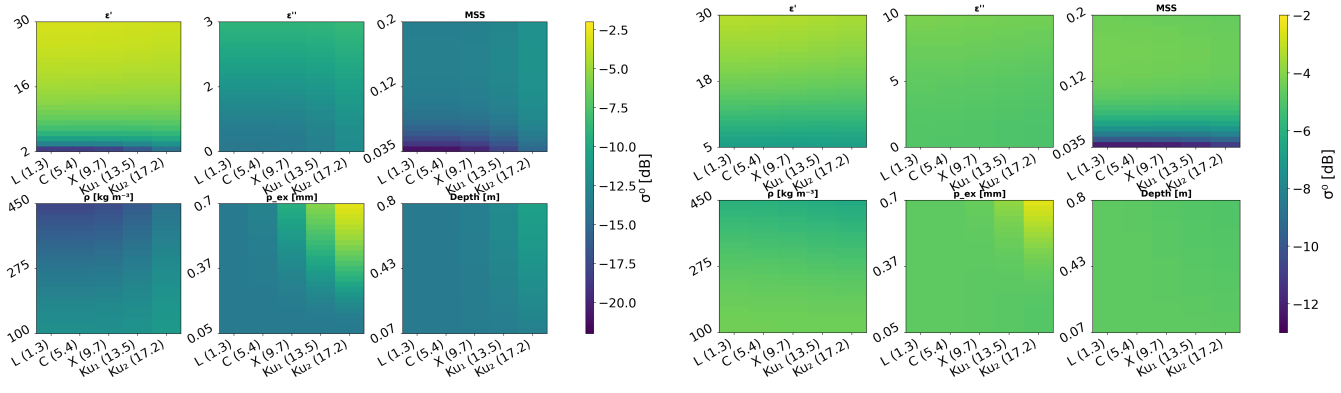

Figure 10. Frequency-parameter response surfaces for the one-at-a-time analysis under frozen (left) and unfrozen (right) soil states. Each panel shows the response to one varied parameter while the single-layer snowpack remains at baseline conditions.

https://doi.org/10.5194/egusphere-2026-656
Preprint. Discussion started: 22 May 2026

can lead to overestimation of the dielectric constant (Gélinas et al., 2025). Nonetheless, Figure 4 shows that it is possible to invert soil properties at a given frequency with good accuracy (RMSE $= 1.25\,\mathrm{dB}$). This study confirms the challenges of scaling ground observations to the scales of different platforms.

The study highlight the relevance of using a model-based inversion approach to estimate effective soil parameters at the scale of the radar observations. By optimizing the soil parameters to best fit the SAR observations, the inverted parameters can be considered as effective parameters that represent the soil conditions at the scale of the radar measurements.

5.3 Effective roughness

An important part of this study was to evaluate the possibility of inverting a single soil roughness parameter that would represent the soil surface conditions for the multiple radar instruments considered. Accounting for the variability and complexity of soil surfaces for the study site in Powassan, it was important to leave the optimization boundaries sufficiently open to represent these variations.

Figure 6 shows that the inverted soil roughness values are in the same order of magnitude as those derived from the LiDAR data, although discrepancies remain. This suggests that the scales captured by the LiDAR data may not fully represent the effective roughness perceived by the SAR instruments, and thus the $\mathrm{MSS}_{\mathrm{inv}}$ values can be considered as an effective roughness parameter. Several factors could explain the discrepancies observed between the inverted roughness values and those derived from the LiDAR data. First, since the SAR penetration depth varies with the permittivity of the soil and the frequency (Ulaby et al., 1982), the effective roughness perceived by the radar signal could be affected by both. This means that the soil roughness sensed by the SAR instruments may differ from that measured by the LiDAR, which only captures the surface topography. Indeed, the majority of the fields were covered with overlying vegetation, therefore the roughness parameters retrieved by LiDAR may not capture the fine scale roughness within the soil that affects the SAR signal. Another factor to consider is the nature of the bottom layer of the snowpack at the time of the campaign. Figure 6 includes coloration based on the snowpack bottom layer density measured in the snowpit during the early March campaign, as well as the grain type of the bottom layer. It appears that sites with a higher bottom layer density that were either melt-freeze crusts or ice layers tend to have higher $\mathrm{MSS}_{\mathrm{inv}}$ values compared to the LiDAR-derived values. This further supports the idea that inverted values represent an effective version of the ground-based measurements, which has the added ability of being able to dynamically adapt and account for local changes to surface roughness that may change overtime.

In the work of Montpetit et al. (2024), the inverted soil roughness values were found to be centered around $\mathrm{MSS}_{\mathrm{inv}} = 0.01$ with very little variation for the TVC tundra site. This value is lower than those found in this study for the Powassan site, which is likely due to the agricultural versus tundra environments. Another study by Meloche et al. (2021) used *Structure from Motion* (SfM) to invert soil roughness from a camera operating in the visible spectrum over multiple sites in the Canadian Arctic near Cambridge Bay (Nunavut) and compared them with inverted roughness values using the geometrical optics formulation. They reported that field measured values were lower compared to roughness values obtained from an inversion algorithm based on passive microwave. Lee and Walker (2022) used an approach similar to the one presented in this study to invert soil roughness

https://doi.org/10.5194/egusphere-2026-656
Preprint. Discussion started: 22 May 2026

from Sentinel-1 SAR data over agricultural fields in Southern Australia. They found a value of $MSS_{inv} = 0.18$ which is consistent with the roughness values presented in this study. However, their study was conducted in an area without snow cover.

5.4 Sensitivity analysis

The sensitivity analysis presented in Figure 7 provides insights into the relative influence of soil parameters on the backscattering coefficient at different radar frequencies and polarizations. The results indicate that the soil roughness MSS_{inv} has the highest influence on the backscattering coefficient for CryoSAR L-band SAR, particularly in VV polarization. This suggests that at L-band frequencies, the surface roughness plays a significant role in determining the backscattering characteristics. For the RCM and TSX, the real part of the soil permittivity (ε') has a more significant impact on the backscattering, especially in HH polarization.

This is further supported by the grid type sensitivity analysis presented in Figure 8. Indeed, the sensor lines in the heatmaps show the range of real permittivity, where the lines represent the maximum value that was reached during the optimization process for the different radar frequencies used in this study. The heatmaps show that for RCM and TSX, there is little variation in the backscattering coefficient along the y-axis (soil roughness MSS_{inv}). The greater variation happens along the x-axis (real part of the soil permittivity ε'). This indicates that for these higher frequency radars, the backscatter signal is more sensitive to changes in soil permittivity than to changes in surface roughness. For CryoSAR, the heatmaps show a more balanced sensitivity to both parameters with variation in backscattering coefficient along both axes. Future inversion studies could consider these sensitivity results to prioritize which parameters to optimize based on the radar frequency and polarization being used.

The one-at-a-time sensitivity analysis links these soil-focused results to the Powassan configuration considered here and to its relevance for TSMM. Under these temperate snow and variable soil conditions, the lower-frequency inversions constrain the soil background, but they do not fully determine the Ku-band response. For this specific configuration, increasing frequency shifts the simulated backscatter sensitivity toward snow microstructure and, more weakly, snow depth. This supports a two-step retrieval strategy for Powassan. Lower-frequency observations first constrain the soil background. Ku-band observations can then be interpreted with a stronger focus on snow properties. This hierarchy should therefore be interpreted for the Powassan case rather than as a general ordering for all snow and soil conditions. Different snowpacks and more stable soil regimes, such as those considered by Montpetit et al. (2024, 2025), may lead to a different sensitivity balance.

The clearest snow response is associated with the exponential correlation length p_{ex}. Its sensitivity increases toward Ku_1 and Ku_2, which makes it a more realistic inversion target than snow density in this experiment. Snow depth follows the same tendency but with a weaker signal. Density remains poorly conditioned because its response is negative under frozen soil and weak under unfrozen wet soil. This interpretation is consistent with Montpetit et al. (2013), who showed that permittivity contrasts between layers can strongly affect the microwave response of layered snowpacks. It should therefore be constrained with ancillary information rather than retrieved alone.

These results extend the tundra-based approach of Montpetit et al. (2024) to a more variable temperate agricultural site. At Powassan, the soil alternated between frozen and unfrozen states, which makes the lower-frequency soil constraint more difficult. This variability also makes the constraint more important. For TSMM, the added value of the approach is therefore not

https://doi.org/10.5194/egusphere-2026-656
Preprint. Discussion started: 22 May 2026

limited to retrieving effective soil parameters. It also identifies which snow properties can realistically be targeted once the soil contribution has been decoupled.

5.5 TSMM perspective

This study shows that it is possible to retrieve soil properties under the snow cover using lower-frequency SAR measurements with good accuracy. Together, the inversion and one-at-a-time sensitivity analysis suggest that this soil constraint is a necessary first step before Ku-band SWE retrieval can be performed in Powassan. The method described by Montpetit et al. (2024) can therefore be applied outside tundra conditions, but the propagation of effective soil parameters toward Ku-band must be treated carefully in temperate environments. By estimating the soil properties first, retrieval algorithms can reduce the dimensionality of the subsequent snow inversion and focus on the snow parameters that dominate the Ku-band response (Montpetit et al., 2025).

5.6 Limitations

While this study demonstrates the feasibility of inverting soil parameters under snow cover using multi-frequency SAR data, several limitations should be acknowledged. First, the inversion approach relies on the accuracy of the SMRT model, which may have inherent limitations in representing complex soil and snow interactions. Picard et al. (2018) mentioned that more work is required in SMRT to correctly represent snow on the ground in active microwave remote sensing since current model formulations are primarily designed for passive microwave applications. The simplified one-at-a-time experiment is also limited by the validity range of the IBA formulation. The largest correlation lengths observed in the Powassan snowpits approach this limit at Ku_2, so the strongest microstructure responses should be interpreted cautiously. The geometrical optics representation of the soil surface scattering implemented in SMRT and used for this study is primarily valid for very rough surfaces compared to the radar wavelength. Some surfaces in this study might not fully meet this criterion, especially at lower frequencies such as the L-band for surfaces with low MSS values. This further explains the difference between the L-band optimization and the C- and X-bands. Another limitation lies in the temporal mismatch between the SAR acquisitions and the ground-based measurements. Although efforts were made to minimize this mismatch by selecting SAR acquisitions close to the March 1st field site visit, soil and snow conditions can change rapidly due to weather events, potentially affecting the accuracy of the comparisons.

5.7 Future work

Because the snow sensitivity analysis remained diagnostic, the next step is to test whether the Powassan dataset can be used to retrieve snow parameters from the CryoSAR Ku-band data. This would involve using the low-frequency inverted soil parameters as inputs and optimizing snow parameters with a similar inversion approach as Montpetit et al. (2025). The full approach was demonstrated by Montpetit et al. (2024, 2025) in a tundra environment, and applying it to the Powassan site would further validate its usage across different biomes. Additionally, future work will explore the application of this inversion methodology to other sites with varying soil types, climate conditions, and more challenging topographies (mountainous regions, boreal forests,

https://doi.org/10.5194/egusphere-2026-656
Preprint. Discussion started: 22 May 2026

etc.) to further test the robustness of the approach. Finally, the ability of surface scattering models to represent the cross-polarized signal will be investigated, and the same inversion methodology will be applied to optimize the SAR backscatter.

6 Conclusions

This study applied a soil microwave parameter inversion methodology using the Snow Microwave Radiative Transfer model to an agro-forested site dataset from the 2022/2023 winter season, building upon the previous work conducted in a tundra environment by Montpetit et al. (2024). The inversion of soil roughness and permittivity using multi-frequency radar data from Cryospheric SAR, Radarsat Constellation Mission, and TerraSAR-X demonstrated the capability of the approach to accurately reproduce the observed backscattering signals across different frequencies with $R^2 \geq 0.74$, RMSE$\leq 1.52\,\mathrm{dB}$ and low bias from the model. The study also highlighted the importance of constraining the soil background parameters for accurate interpretation of Ku-band backscatter in temperate snow-covered environments, where soil conditions can be highly variable due to freeze-thaw cycles and moisture changes. These results highlight its potential usage for future satellite missions operating at different frequencies, such as Terrestrial Snow Mass Mission.

Base on this work, future inversion frameworks should explicitly represent the time-evolving soil background permittivity (freeze/thaw and moisture-driven dielectric changes), since assuming a static soil state can bias retrievals in rapidly varying temperate conditions. Considering a single soil roughness value throughout the winter season is also recommended where no significant disturbance (plowing, excavating, etc.) is observed. To further test the approach and improve our understanding of soil and snow interactions with radar signals, future work will look at applying the methodology to different sites with varying soil types, climate conditions and topographies.

Finally, this study highlights the reliability of the soil parameter inversion approach using SMRT across different environments and soil conditions. The successful application of this methodology to the Powassan site demonstrates its potential for broader applications in snow monitoring and remote sensing.

Author contributions. AG wrote the original draft and performed the analysis. AG, BM, and AR conceptualized the study. BM, JM, and PT contributed to methodology and data collection. ZA, WW, and RK provided CryoSAR data. AL and AR supervised the project. All authors reviewed and edited the manuscript.

Competing interests. At least one of the (co-)authors is a member of the editorial board of The Cryosphere.

Acknowledgements. OpenAI's ChatGPT, Anthropic's Claude and Google's Gemini were used in this work as assistance in the writing and editing process. The authors would like to acknowledge the financial support of the CSA FAST 2019 Grant No. 19FAWATA23, the Natural Sciences and Engineering Research Council of Canada (NSERC), the Fonds de recherche du Québec – Nature et technologies (FRQNT)

https://doi.org/10.5194/egusphere-2026-656
Preprint. Discussion started: 22 May 2026

and the Fonds de collaboration et d'innovation (FCI). The authors would like to thank everyone involved in the data collection campaigns at Powassan, including the teams from Environment and Climate Change Canada, the University of Waterloo, the Université de Sherbrooke, and the Université du Québec à Trois-Rivières as well as Arvids Silis and Micheal Davey from ECCC. The authors also thank the Centre d'études nordiques (CEN) for funding opportunities. Special thanks go to Markus Wand at Wand Family Farm, who allowed us access to their lands for field measurements and assisted us during the multiple field visits.

https://doi.org/10.5194/egusphere-2026-656
Preprint. Discussion started: 22 May 2026

References

Aygün, O., Kinnard, C., and Campeau, S.: Impacts of climate change on the hydrology of northern midlatitude cold regions, Progress in Physical Geography: Earth and Environment, 44, 338–375, https://doi.org/10.1177/0309133319878123, 2020.

Belinska, K., Fischer, G., Parrella, G., and Hajnsek, I.: The Potential of Multifrequency Spaceborne DInSAR Measurements for the Retrieval of Snow Water Equivalent, IEEE Journal of Selected Topics in Applied Earth Observations and Remote Sensing, 17, 2950–2962, https://doi.org/10.1109/JSTARS.2023.3345139, 2023.

Bircher, S., Demontoux, F., Razafindratsima, S., Zakharova, E., Drusch, M., Wigneron, J.-P., Kerr, Y. H., Bircher, S., Demontoux, F., Razafindratsima, S., Zakharova, E., Drusch, M., Wigneron, J.-P., and Kerr, Y. H.: L-Band Relative Permittivity of Organic Soil Surface Layers—A New Dataset of Resonant Cavity Measurements and Model Evaluation, Remote Sensing, 8, https://doi.org/10.3390/rs8121024, 2016.

Brangers, I., Marshall, H.-P., De Lannoy, G., Dunmire, D., Mätzler, C., and Lievens, H.: Tower-based C-band radar measurements of an alpine snowpack, The Cryosphere, 18, 3177–3193, https://doi.org/10.5194/tc-18-3177-2024, 2024.

Chabot, M., Lindsay, J., Rowlandson, T., and Berg, A. A.: Comparing the Use of Terrestrial LiDAR Scanners and Pin Profilers for Deriving Agricultural Roughness Statistics, Canadian Journal of Remote Sensing, 44, 153–168, https://doi.org/10.1080/07038992.2018.1461559, 2018.

Derksen, C., Lemmetyinen, J., King, J., Belair, S., Garnaud, C., Lapointe, M., Crevier, Y., Burbidge, G., and Siqueira, P.: A Dual-Frequency Ku-Band Radar Mission Concept for Seasonal Snow, Tech. Rep. providing, https://doi.org/10.1109/igarss.2019.8898030, 2019.

Dobson, M., Ulaby, F., Hallikainen, M., and El-rayes, M.: Microwave dielectric behavior of wet soil-part II: dielectric mixing models, IEEE Transactions on Geoscience and Remote Sensing, GE-23, 35–46, https://doi.org/10.1109/tgrs.1985.289498, 1985.

Duguay, Y. and Bernier, M.: The Use of RADARSAT-2 and TerraSAR-X Data for the Evaluation of Snow Characteristics in Subarctic Regions, IEEE International Geoscience and Remote Sensing Symposium, pp. 3556–3559, https://doi.org/https://doi.org/10.1109/IGARSS.2012.6350650, 2012.

Gallet, J.-C., Domine, F., Zender, C. S., and Picard, G.: Measurement of the specific surface area of snow using infrared reflectance in an integrating sphere at 1310 and 1550 nm, The Cryosphere, 3, 167–182, https://doi.org/10.5194/tc-3-167-2009, 2009.

Garnaud, C., Bélair, S., Carrera, M. L., Derksen, C., Bilodeau, B., Abrahamowicz, M., Gauthier, N., and Vionnet, V.: Quantifying Snow Mass Mission Concept Trade-Offs Using an Observing System Simulation Experiment, Journal of Hydrometeorology, 20, 155–173, https://doi.org/10.1175/jhm-d-17-0241.1, 2019.

Goodrich, L. E.: The influence of snow cover on the ground thermal regime, Canadian Geotechnical Journal, 19, 421–432, https://doi.org/10.1139/t82-047, 1982.

Gélinas, A., Filali, B., Langlois, A., Kelly, R., Mavrovic, A., Demontoux, F., and Roy, A.: New Wideband Large Aperture Open-Ended Coaxial Microwave Probe for Soil Dielectric Characterization, IEEE Transactions on Geoscience and Remote Sensing, 63, 1–8, https://doi.org/10.1109/TGRS.2025.3539532, 2025.

Herman, J. and Usher, W.: SALib: An open-source Python library for Sensitivity Analysis, The Journal of Open Source Software, 2, https://doi.org/10.21105/joss.00097, 2017.

Iwanaga, T., Usher, W., and Herman, J.: Toward SALib 2.0: Advancing the accessibility and interpretability of global sensitivity analyses, Socio-Environmental Systems Modelling, 4, 18 155, https://doi.org/10.18174/sesmo.18155, 2022.

https://doi.org/10.5194/egusphere-2026-656
Preprint. Discussion started: 22 May 2026

Kelly, R., Thompson, A., Wang, W., Akhavan, Z., Welch, J., Toose, P., Derksen, C., Montpetit, B., and Meta, A.: The Airborne Cryospheric SAR System (CryoSAR): Characterizing Cold Season Hydrology Using Ku and L-Band Polarimetric SAR Observations, in: IGARSS 2024 - 2024 IEEE International Geoscience and Remote Sensing Symposium, pp. 6559–6561, ISSN 2153-7003, https://doi.org/10.1109/IGARSS53475.2024.10642350, iSSN: 2153-7003, 2024.

King, J., Derksen, C., Toose, P., Langlois, A., Larsen, C., Lemmetyinen, J., Marsh, P., Montpetit, B., Roy, A., Rutter, N., and Sturm, M.: The influence of snow microstructure on dual-frequency radar measurements in a tundra environment, Remote Sensing of Environment, 215, 242–254, https://doi.org/10.1016/j.rse.2018.05.028, 2018.

Lee, J. H. and Walker, J.: Inversion of soil roughness for estimating soil moisture from time-series Sentinel-1 backscatter observations over Yanco sites, Geocarto International, 37, 1850–1862, https://doi.org/10.1080/10106049.2020.1805030, 2022.

Lemmetyinen, J., Derksen, C., Rott, H., Macelloni, G., King, J., Schneebeli, M., Wiesmann, A., Leppänen, L., Kontu, A., and Pulliainen, J.: Retrieval of Effective Correlation Length and Snow Water Equivalent from Radar and Passive Microwave Measurements, Remote Sensing, 10, https://doi.org/10.3390/rs10020170, 2018.

Lemmetyinen, J., Cohen, J., Kontu, A., Vehviläinen, J., Hannula, H.-R., Merkouriadi, I., Scheiblauer, S., Rott, H., Nagler, T., Ripper, E., Elder, K., Marshall, H.-P., Fromm, R., Adams, M., Derksen, C., King, J., Meta, A., Coccia, A., Rutter, N., Sandells, M., Macelloni, G., Santi, E., Leduc-Leballeur, M., Essery, R., Menard, C., and Kern, M.: Airborne SnowSAR data at X and Ku bands over boreal forest, alpine and tundra snow cover, Earth System Science Data, 14, 3915–3945, https://doi.org/https://doi.org/10.5194/essd-14-3915-2022, 2022.

Lindsay, J.: Whitebox GAT: A case study in geomorphometric analysis, Computers & Geosciences, 95, 75–84, https://doi.org/https://doi.org/10.1016/j.cageo.2016.07.003, 2016.

Meloche, J., Royer, A., Langlois, A., Rutter, N., and Sasseville, V.: Improvement of microwave emissivity parameterization of frozen Arctic soils using roughness measurements derived from photogrammetry, International Journal of Digital Earth, 14, 1380–1396, https://doi.org/10.1080/17538947.2020.1836049, 2021.

Mironov, V. L., De Roo, R. D., and Savin, I. V.: Temperature-Dependable Microwave Dielectric Model for an Arctic Soil, IEEE Transactions on Geoscience and Remote Sensing, 48, 2544–2556, https://doi.org/10.1109/TGRS.2010.2040034, 2010.

Montpetit, B., Royer, A., Langlois, A., Cliche, P., Roy, A., Champollion, N., Picard, G., Domine, F., and Obbard, R.: New shortwave infrared albedo measurements for snow specific surface area retrieval, Journal of Glaciology, 58, 941–952, https://doi.org/10.3189/2012JoG11J248, 2012.

Montpetit, B., Royer, A., Roy, A., Langlois, A., and Derksen, C.: Snow microwave emission modeling of ice lenses within a snowpack using the microwave emission model for layered snowpacks, IEEE Transactions on Geoscience and Remote Sensing, 51, 4705–4717, 2013.

Montpetit, B., King, J., Meloche, J., Derksen, C., Siqueira, P., Adam, J. M., Toose, P., Brady, M., Wendleder, A., Vionnet, V., and Leroux, N. R.: Retrieval of snow and soil properties for forward radiative transfer modeling of airborne Ku-band SAR to estimate snow water equivalent: the Trail Valley Creek 2018/19 snow experiment, The Cryosphere, 18, 3857–3874, https://doi.org/10.5194/tc-18-3857-2024, 2024.

Montpetit, B., Meloche, J., Vionnet, V., Derksen, C., Wooley, G., Leroux, N. R., Siqueira, P., Adams, J. M., and Brady, M.: Retrieving Snow Water Equivalent from airborne Ku-band data: The Trail Valley Creek 2018/19 Snow Experiment, EGUsphere, 2025, 1–31, https://doi.org/10.5194/egusphere-2025-2317, 2025.

Mätzler, C. and Wiesmann, A.: Extension of the Microwave Emission Model of Layered Snowpacks to Coarse-Grained Snow, Remote Sensing of Environment, 70, 317–325, https://doi.org/10.1016/S0034-4257(99)00047-4, 1999.

https://doi.org/10.5194/egusphere-2026-656
Preprint. Discussion started: 22 May 2026

NRCan: High Resolution Digital Elevation Model (HRDEM) - CanElevation Series, https://open.canada.ca/data/en/dataset/957782bf-847c-4644-a757-e383c0057995, 2025.

Picard, G., Le Toan, T., Quegan, S., Caraglio, Y., and Castel, T.: Radiative transfer modeling of cross-polarized backscatter from a pine forest using the discrete ordinate and eigenvalue method, IEEE Transactions on Geoscience and Remote Sensing, 42, 1720–1730, https://doi.org/10.1109/TGRS.2004.831229, 2004.

Picard, G., Brucker, L., Roy, A., Dupont, F., Fily, M., Royer, A., and Harlow, C.: Simulation of the microwave emission of multi-layered snowpacks using the Dense Media Radiative transfer theory: the DMRT-ML model, Geoscientific Model Development, 6, 1061–1078, https://doi.org/10.5194/gmd-6-1061-2013, 2013.

Picard, G., Sandells, M., and Löwe, H.: SMRT: an active–passive microwave radiative transfer model for snow with multiple microstructure and scattering formulations (v1.0), Geoscientific Model Development, 11, 2763–2788, https://doi.org/10.5194/gmd-11-2763-2018, 2018.

Picard, G., Löwe, H., and Mätzler, C.: Brief communication: A continuous formulation of microwave scattering from fresh snow to bubbly ice from first principles, The Cryosphere, 16, 3861–3866, https://doi.org/10.5194/tc-16-3861-2022, 2022.

Proksch, M., Löwe, H., and Schneebeli, M.: Density, specific surface area, and correlation length of snow measured by high-resolution penetrometry, Journal of Geophysical Research: Earth Surface, 120, 346–362, https://doi.org/10.1002/2014JF003266, 2015.

Pulliainen, J., Luojus, K., Derksen, C., Mudryk, L., Lemmetyinen, J., Salminen, M., Ikonen, J., Takala, M., Cohen, J., Smolander, T., and Norberg, J.: Patterns and trends of Northern Hemisphere snow mass from 1980 to 2018, Nature, 581, 294–298, https://doi.org/10.1038/s41586-020-2258-0, 2020.

Rutter, N., Sandells, M. J., Derksen, C., King, J., Toose, P., Wake, L., Watts, T., Essery, R., Roy, A., Royer, A., Marsh, P., Larsen, C., and Sturm, M.: Effect of snow microstructure variability on Ku-band radar snow water equivalent retrievals, The Cryosphere, 13, 3045–3059, https://doi.org/10.5194/tc-13-3045-2019, 2019.

Sobol', I.: Global sensitivity indices for nonlinear mathematical models and their Monte Carlo estimates, Mathematics and Computers in Simulation, 55, 271–280, https://doi.org/https://doi.org/10.1016/S0378-4754(00)00270-6, the Second IMACS Seminar on Monte Carlo Methods, 2001.

Tsang, L., Durand, M., Derksen, C., Barros, A. P., Kang, D.-H., Lievens, H., Marshall, H.-P., Zhu, J., Johnson, J., King, J., Lemmetyinen, J., Sandells, M., Rutter, N., Siqueira, P., Nolin, A., Osmanoglu, B., Vuyovich, C., Kim, E., Taylor, D., Merkouriadi, I., Brucker, L., Navari, M., Dumont, M., Kelly, R., Kim, R. S., Liao, T.-H., Borah, F., and Xu, X.: Review article: Global monitoring of snow water equivalent using high-frequency radar remote sensing, The Cryosphere, 16, 3531–3573, https://doi.org/10.5194/tc-16-3531-2022, 2022.

Ulaby, F. T., Moore, R. K., and Fung, A. K.: Microwave remote sensing: Active and passive. Volume 2-Radar remote sensing and surface scattering and emission theory, 1982.

Vionnet, V., Mortimer, C., Brady, M., Arnal, L., and Brown, R.: Canadian historical Snow Water Equivalent dataset (CanSWE, 1928–2020), Earth System Science Data, 13, 4603–4619, https://doi.org/10.5194/essd-13-4603-2021, 2021.

Zhang, T.: Influence of the seasonal snow cover on the ground thermal regime: An overview, Reviews of Geophysics, 43, https://doi.org/10.1029/2004RG000157, 2005.